Della Ragione, G. *et al.* (2024). *Géotechnique* **74**, No. 12, 1329–1342 [https://doi.org/10.1680/jgeot.22.00241]

Numerical investigation of fibre-optic sensing for sinkhole detection

GIANLUIGI DELLA RAGIONE*, EMILIO BILOTTA†, XIAOMIN XU‡, TALIA S. DA SILVA BURKE§, TOBIAS MÖLLER‖ and CHRISTELLE N. ABADIE¶

This paper forms part of the SINEW (sinkhole early warning) project and continues the work conducted by Möller and co-workers in 2022, where 1***g*** experiments demonstrated the feasibility of using distributed fibre-optic sensing (DFOS) for sinkhole early warning. Their experimental campaign highlighted an order of magnitude difference in the strain between the soil and the cable that remains unexplained and weakens confidence in the technology and/or the experimental method. This paper uses three-dimensional finite-element analyses to examine further this discrepancy and the soil–cable interface. The results support the experimental findings and demonstrate that the DFOS signature strain profile is induced by the horizontal movement of the ground, and enhanced when sufficient coupling at the soil–cable interface is achieved. This result holds when modelling is scaled to realistic confining pressure, and its significance is twofold. First, this needs to be accounted for in the DFOS laying technique. Second, particles of cohesionless soils undergo relatively high horizontal displacement away from the centre of the sinkhole, and this means that DFOS cables are able to detect subsidence away from the centre of the sinkhole. The paper illustrates this result and the signature strain profile expected in this case.

KEYWORDS: computational geotechnics; fibre-optic monitoring; finite-element analysis; geohazards; ground movements; sensors; subsidence

INTRODUCTION

Sinkholes are a common geohazard consisting of a hole or depression formed in the ground surface due to the subsurface collapse of a cavity (Jennings *et al.*, 1965). They are commonly caused by the dissolution of carbonate rocks such as limestone, dolomites, gypsum or chalk (Cooper *et al.*, 2011), but can be caused by the collapse of human-made structures such as old mine shafts (Brady & Brown, 1993) or buried pits in urban areas, in many cases due to erosion from leaking utility lines. In the built environment, sinkholes have the potential to cause severe damage to infrastructure, and in some cases lead to casualties.

Sinkholes can develop over long periods, thus allowing ground deformation to be measured well before their eventual collapse (Chang & Hanssen, 2014). A range of methods have been explored, aiming to measure ground settlements to detect possible sinkhole formation sufficiently in advance. For example, electrical resistivity imaging (Van Schoor, 2002; Youssef *et al.*, 2012), two-dimensional (2D) full seismic waveform tomography (Tran *et al.*, 2013), multi-temporal interferometric synthetic aperture radar (InSAR) (Chang & Hanssen, 2014) or thermal far-infrared imagining (Lee *et al.*, 2016). However, these techniques cannot accommodate the temporal frequency needed while also offering large area coverage with sufficient sampling resolution (Möller *et al.*, 2022); as a result, there are limitations to wide-scale adoption in practice.

Pioneer full-scale experiments on the use of fibre-optic sensors for sinkhole detection in sands were carried out by Villard & Briançon (2008). A 2 m wide and 0·5 m depth void was simulated with inflatable balloons, and monitoring was carried out with 1 m spaced fibre Bragg gratings (FBGs) incorporated in a fibre-optic cable, woven in a geosynthetic sheet. In their study, the focus was on the evaluation of strain developed into the geotextile. The study clearly showed that the fibre-optic sensor was able to pick up strain from the beginning of the balloons' deflation, with geosynthetics placed directly above the balloons. Similar tests, involving the use of a 0·5 m wide inflatable balloon, were performed a year later by Belli *et al.* (2009). Fibre-optic strains were retrieved based on Brillouin scattering with a spatial resolution of 1 m. Three different fibre-optic sensors were used, both independently and as part of a geogrid, in order to study the sensitivity of the sensors in detecting soil settlements. A recent development in sinkhole detection relies on the use of fibre-optic cables, included in the earthwork during construction, sometimes within the use of a geogrid, to monitor ground displacements (Guan *et al.*, 2013, 2015; Klar *et al.*, 2014; Zhang *et al.*, 2016; Inaudi, 2017). This is particularly adapted for long linear infrastructure, such as railways or roads. For this purpose, Xu *et al.* (2022a) extended the research to the use of fibre optics within a geogrid, with a similarly successful outcome. Lanticq *et al.* (2009) performed a full-scale test, simulating the formation of two voids 2·1 m wide and 2 m deep, sufficiently spaced to avoid interference. The first embankment was softer than the second in order to study the influence of soil properties. A cable 2 mm in diameter containing eight optical fibres was analysed with Brillouin optical time-domain reflectometry (BOTDR) and optical frequency-domain reflectometry (OFDR), to study the efficacy of both technologies in

Manuscript received 3 August 2022; revised manuscript accepted 12 January 2023. First published online ahead of print 13 February 2023.
Discussion on this paper is welcomed by the editor.
* Department of Civil, Architectural and Environmental Engineering, University of Naples, Naples, Italy (former visiting researcher at CSIC) (Orcid:0000-0002-2434-1438).
† Department of Civil, Architectural and Environmental Engineering, University of Naples, Naples, Italy (Orcid:0000-0002-3185-2738).
‡ Cambridge Centre for Smart Infrastructure and Construction (CSIC), Department of Engineering, University of Cambridge, Cambridge, UK (Orcid:0000-0002-1255-9026).
§ Department of Civil Engineering, University of Pretoria, Pretoria, South Africa (Orcid:0000-0001-9393-8601).
‖ Department of Engineering, University of Cambridge, Cambridge, UK (Orcid:0000-0002-9497-2729).
¶ Department of Engineering, University of Cambridge, Cambridge, UK (Orcid:0000-0002-5586-6560).

detecting soil strains. Finite-element numerical analysis (FEA) was also carried out, and the results were in agreement with monitored data, indicating that, due to higher spatial resolution, OFDR technology was to be preferred. However, this conclusion needs to be extended moving forward to new technological developments in fibre-optic sensing (Brillouin optical time-domain analysis (BOTDA) and Brillouin optical frequency-domain analysis (BOFDA)) (Sparrevik *et al.*, 2022).

An additional few field studies were later published in the literature on the use of distributed fibre-optic sensing (DFOS) for sinkhole detection (Guan *et al.*, 2013; Buchoud *et al.*, 2016; Inaudi, 2017). However, to date, there is no rigorous understanding of the recorded signature strain profile, derived from systematic experiments in controlled and repeatable conditions in the laboratory, and fully comprehended by way of numerical analyses.

This paper is part of the ongoing SINEW (sinkhole early warning) project and extends the results of experimental tests carried out at the Schofield Centre in Cambridge (UK), and presented in a separate paper by Möller *et al.* (2022). In that work, the strains of DFOS cables embedded in a cohesionless soil layer at 1$\boldsymbol{g}$ were measured while lowering a trapdoor, representing the progressive formation of a sinkhole. A clear signature strain profile, capturing the early stages of the formation of a sinkhole, was outlined. A procedure to assess the position of the sinkhole and the extent of its effects at the ground surface was also proposed. However, doubts remained as to the pertinence of scaling the experimental results for large-scale practice. In particular, the experiments from Möller *et al.* (2022) are not suited to elucidate further the effects of the soil–cable interface and stress level on the cable response for large-scale applications (Xu *et al.*, 2022b). This is the purpose of the present paper.

Here, a series of three-dimensional (3D) FEAs are presented to further the understanding from Möller *et al.* (2022), and scale the results up to more realistic stress levels. First, the 1$\boldsymbol{g}$ experiments are reproduced and validated by comparing particle image velocimetry (PIV) experimental results with numerical FEA output. The numerical results are then used to check the compatibility of the experimental cable's strain profiles from DFOS against the numerical cable model. Once validated, the model is used to focus on the cable's interface behaviour. This study also offers the possibility of discussing the difficulties in establishing a robust constitutive model for cohesionless soils at low confining pressure, a generally acknowledged limitation in numerical modelling in geotechnics. Following this work, the finite-element model is carefully scaled up to realistic stress levels, reproducing one of the centrifuge tests in da Silva (2017). This test involved the formation of a sinkhole of the same geometry as that performed by Möller *et al.* (2022), with an enhanced gravity of 40$\boldsymbol{g}$, but did not include fibre-optic cables. The settlement data published by da Silva (2017) are used for validation of the 3D FE model and a prediction is made as to what the signature strain profile would have been if fibre-optic sensing had been used in this test. The method outlined by Möller *et al.* (2022) is used to predict the sinkhole size and location and soil–cable coupling. The final analysis extends the findings from the above 2D experiments to applications in three dimensions, considering the case where cables are not laid directly above the centre of the sinkhole. The results further support that deploying DFOS in the construction of critical infrastructure would enable early detection of sinkhole formation.

EXPERIMENTAL BENCHMARK

Tests with DFOS cables

The benchmark experimental study was carried out by Möller *et al.* (2022) using a 790 × 200 × 200 mm rectangular rig, equipped with a trapdoor of width, $B = 100$ mm, that can mimic the formation of a sinkhole within a single soil layer (Fig. 1). The soil samples were prepared using dry Hostun sand (Table 1), with a model height of $H = 200$ mm ($H/B = 2$).

Seven models were prepared at increasing relative densities, ranging from $D_R = 20\%$ to $D_R = 88\%$ (Möller *et al.*, 2022), to compare and understand the influence of different soil conditions. The fibre-optic cables were installed in the soil body at three nominal heights of 50, 100 and 150 mm above the trapdoor (termed bottom, central and top cable, respectively) with the locations highlighted using dyed black sand (Fig. 1). The cable was laid so as to avoid any pre-stress, and was pinned on the vertical walls of the rig. Images for the PIV analysis were acquired using two Canon Powershot G10 cameras and the analysis was carried out using GeoPIV_RG (Stanier *et al.*, 2016). The trapdoor displacement, δ, was recorded using two linear variable differential transformers located below the trapdoor. Data from DFOS cables were collected using the Luna ODiSi 6100 analyser (Luna Innovations, 2020), which is based on the measurement of Rayleigh back-scatter light in the fibre-optic cables. The fine resolution of the analyser, ranging from one sampled point every 0·65 mm up to 2·65 mm, enables the accurate monitoring of small-scale experiments. Further details of the experimental campaign can be found in the paper by Möller *et al.* (2022).

Soil arching around the trapdoor allows the ground to redistribute stresses to bear the overburden load. Initially, as the trapdoor starts moving, there is a sharp decrease in load on the trapdoor to a minimum value. This is called the maximum arching phase and occurs for a trapdoor displacement equal to 1–2% of its width (Iglesia *et al.*, 2014; da Silva Burke & Elshafie, 2021). The experimental results from Möller *et al.* (2022) show that the fibre-optic cables are able to detect a signal in this early phase of the sinkhole

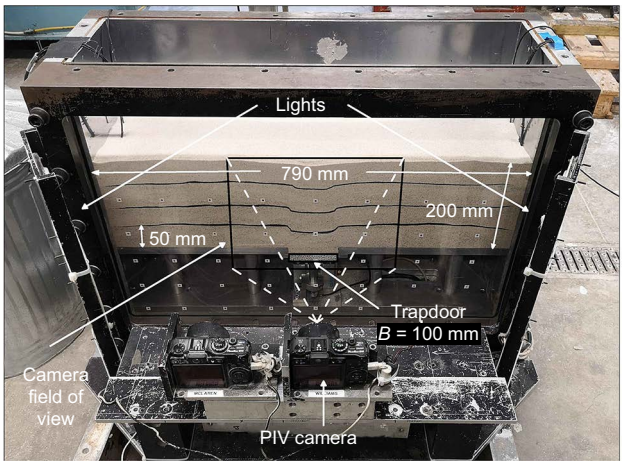

Fig. 1. Photograph of the experimental set-up for the 1g tests

Table 1. Hostun sand properties (da Silva Burke and Elshafie, 2021)

Property	Symbol	Units	Value
Average particle size	d_{50}	mm	0·356
Minimum void ratio	e_{min}	—	0·555
Maximum void ratio	e_{max}	—	1·010
Specific gravity	G_s	—	2·65
Critical angle of friction	ϕ'_c	degrees	34

formation, with a clear signature of the strain that enables the sinkhole to be monitored well before further progressive movement to the surface and/or collapse. It was shown that the fibre-optic data could be used to detect the trapdoor position and provide a conservative estimation of its width; this is analogous to detecting sinkhole location and size. However, with varying interface conditions between the fibre-optic cable and the soil, the strains measured by the cable differed from those measured with PIV. Further experimental investigation could not enable further understanding of this phenomenon, as the PIV data correspond to sample strain against the window, and thus far from the cable located in the body of the soil sample. Moreover, the soil stresses at 1***g*** are significantly lower than stresses in real conditions, which may affect shear band formation and coupling between the soil and the fibre-optic cable. Such issues are investigated in this paper by way of FEAs, in order to assess their relevance in possible application to real cases.

Centrifuge test with no DFOS cable

To enable robust scaling of the 1***g*** test 3D FE model, a centrifuge test from the published literature was selected for validation purposes. This test was performed with the same rig as in Fig. 1, but with a trapdoor width of 50 mm instead of 100 mm (da Silva, 2017). The test was conducted at 40***g*** on the centrifuge at the Schofield Centre, University of Cambridge, UK and is thus representative of a 2 m wide void, 4 m below the ground surface. Fibre-optic sensing cables were not included in this test; soil deformations were monitored using PIV. The main geometrical characteristics of the test are summarised in Table 2.

NUMERICAL MODEL

Geometry and meshing

The experimental tests by Möller *et al*. (2022) were back-analysed by means of 3D FE calculations using the software platform Plaxis 3D (Brinkgreve *et al*., 2015). The numerical model is shown in Fig. 2, representing half the specimen, as per the symmetry at the trapdoor centre. The mesh consists of 305 000 tetrahedral elements with 425 000 nodes. The mesh is denser around the trapdoor and around the cables, where larger deformations are expected (Fig. 2). Three-dimensional analysis permitted the investigation of the role of interface conditions between the soil and the cable by looking at soil stress and strain fields in proximity of the cable that could not be measured in testing.

Trapdoor tests comparing the response of fibre-optic cables to fine- and coarse-grained material were carried out by Blairon *et al*. (2011), showing that the sensitivity of the cable reduces in fine-grained materials, because maximal induced strain is larger in granular material due to arching. In addition, the experiments carried out by Möller *et al*. (2022) and replicated here involve a cable diameter over mean particle size (D/d_{50}) ratio of 5·6, a fairly low value at which the soil should be regarded as a granular media (Taylor, 1994). Nevertheless, this limitation will not apply to cables used in the field, where D/d_{50} will typically be greater than 20 and the soil can be treated as a continuum (Taylor, 1994). Hence, this limitation was ignored in the following, and the soil was considered using continuum mechanics.

The material model selected in this paper for the sand is the hardening soil model with small-strain stiffness ('HSsmall') (Schanz *et al*., 1999; Benz *et al*., 2009). It is an elastic–plastic hardening model, which accounts for soil stiffness decay with shear strain and dependence on the stress level. This model was selected because it offers a good compromise, capturing the behaviour of sands at low confining pressure relatively accurately, while also being able to capture full-scale behaviour, providing a judicious choice of parameter values. At low confining pressures, three conditions of loose (i.e. $D_R = 20\%$), medium dense (i.e. $D_R = 52\%$) and dense sand (i.e. $D_R = 88\%$) were analysed to replicate the 1***g*** tests from Möller *et al*. (2022). At larger stress levels (40***g***), a relative density of $D_R = 87{\cdot}5\%$ was considered for both analyses (2D and 3D) described in this paper to compare with da Silva (2017) test results.

For the 1***g*** experiment, the trapdoor tests were performed on a sand layer of rather low thickness, and the maximum average soil stress at trapdoor level (i.e. 200 mm deep) was very low and approximately equal to 2 kPa. This is a challenge for numerical modelling, as sand at such small confining stresses exhibits higher dilatancy angles and lower compressibility, which is generally ignored in constitutive

Table 2. Centrifuge test properties at prototype scale (da Silva, 2017)

Property	Symbol	Units	Value
Trapdoor width	B	m	2
Sample height	H	m	4
Relative density	D_R	%	87·5
g-level	—	***g***	40

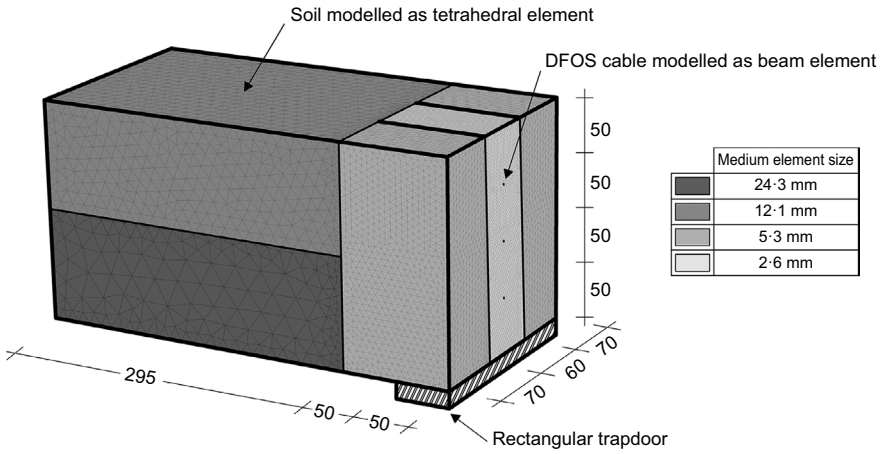

Fig. 2. Plaxis 3D numerical model representing half of the plane-strain problem with soil modelled as tetrahedral element and fibre-optic cable modelled as an embedded beam element (395 × 200 × 200 mm). Dimensions in mm

models. The influence of such a low confining stress on soil dilatancy and on the shear stiffness decay is examined in the following discussion.

Dilatancy at low confining stress

The dilatant behaviour is commonly described by the dilatancy angle ψ (Bolton, 1986)

$$\phi'_p - \phi'_c = 0{\cdot}8\psi_{max} \quad (1)$$

where ϕ'_p and ϕ'_c are the effective peak angle and critical angle of shear resistance, respectively. The dependency of the dilatancy of sand on the mean effective stress p' and the relative density D_R of the soil is taken into account through the relative dilatancy index I_R (Bolton, 1986)

$$I_R = D_R(Q - \ln p') - R \quad (2)$$

where Q and R are two fitting parameters, which are a function of the soil material (Chakraborty & Salgado, 2010). These are commonly set equal to 10 and 1, respectively, to offer a unique relationship for the dilatancy behaviour of the sands considered by Bolton (1986). The difficulty in using this framework, however, is that it was originally validated against data from triaxial compression tests, and therefore even low confining stresses are commonly an order of magnitude above the confining pressure of interest in this paper (typically >20 kPa). Lancelot *et al*. (2006) performed tests on Hostun sand at relatively low confining stresses (20–50 kPa) and showed that the dilatancy angle at such low stresses is indeed stress dependent. Chakraborty & Salgado (2010) also explored low confining stresses (10–50 kPa and above) with Toyoura sand and showed that equation (2) provides a reasonable fit, even at these low confining stresses, with $R = 1$ and $Q \sim 8$ for confining stresses ranging from 10 to 26 kPa. Decreasing the value of Q has the effect of reducing the tendency of the soil to dilate. For the numerical modelling of the 1$\boldsymbol{g}$ tests the aim was to replicate the mechanisms of the soil–cable behaviour and observe if the trends observed experimentally are repeatable in a numerical simulation, most notably considering the order of magnitude strain reduction in the cable compared to the soil and shape of the strain profile. The aim was not to provide exact predictions at these low stresses, which are not representative of full-scale behaviour. For this reason, it was decided to use equation (2) with the original values of $Q = 10$ and $R = 1$ to provide a reasonable estimate of I_R.

The angle of maximum dilation can be estimated according to equation (3) (Schanz & Vermeer, 1996)

$$\psi_{max} = \arcsin\left(\frac{I_{R,f}}{I_{R,f} + 6{\cdot}7}\right) \quad (3)$$

where $I_{R,f}$ is the dilatancy index evaluated at failure (i.e. when $p' = p'_f$). The angle of maximum dilation, ψ_{max}, is a key constitutive parameter in the model selected for this paper, which needs to be assessed independently for each relative density selected for modelling. To this aim, an average value of the mean effective stress p' along the layer thickness was assumed for each of the three cases and the value of the peak friction angle ϕ'_p (equation (1)) was selected in order to keep the same value of the critical friction angle, $\phi'_c = 34°$ (Benz, 2006).

Stiffness decay with strain level at low confining stress

The HSsmall model accounts for the decay of shear stiffness with the shear strain through two parameters: (*a*) the initial shear stiffness modulus G_0 and (*b*) the shear strain level at which the reduction of stiffness modulus is $G/G_0 \approx 0{\cdot}7$, also called $\gamma_{0{\cdot}7}$, which uniquely defines the stiffness decay curve (Benz *et al*., 2009). The initial shear stiffness modulus G_0 of Hostun sand was evaluated according to equation (4) (Oztoprak & Bolton, 2011)

$$G_0 = \frac{5760 p_{atm}}{(1+e)^3}\left(\frac{p'}{p_{atm}}\right)^{0{\cdot}5} \quad (4)$$

where p_{atm} is the atmospheric pressure (i.e. 100 kPa); e is the void ratio, assumed to be constant through the depth of the sand layer; and p' is the target mean stress level.

The material model takes into account the dependency of shear stiffness modulus G_0 on the confining pressure through the following equation

$$G_0 = G_0^{ref}\left(\frac{\sigma'_3}{p_{ref}}\right)^m \quad (5)$$

where G_0^{ref} is the shear stiffness at the reference pressure and can be computed by substituting equation (5) into equation (4), assuming that $p' = \sigma'_3 = p_{ref} = p_{atm} = 100$ kPa.

Experimental evidence has shown that the shear strain level $\gamma_{0{\cdot}7}$ is also a function of the stress level (Darendeli & Stokoe, 2001; Wichtmann & Triantafyllidis, 2004). Unfortunately, the material model does not take this dependence into account. In order to correct for this, equation (6) was used to scale the shear strain level $\gamma_{0{\cdot}7}$ to the appropriate stress level (Darendeli & Stokoe, 2001)

$$\gamma_{0{\cdot}7} = (\gamma_{0{\cdot}7})_{ref}\left(\frac{p'}{p_{ref}}\right)^{0{\cdot}5} \quad (6)$$

where p' is the target stress level; p_{ref} is the reference confining stress level (usually taken as equal to 100 kPa, i.e. atmospheric pressure); and $(\gamma_{0{\cdot}7})_{ref}$ is the shear strain level at the reference confining stress level.

Dependency of the stiffness on the stress at medium to large strain level

HSsmall incorporates power laws to define the dependency of the stiffness parameter at medium to large strains on the confining stress. The soil stiffness is defined through three moduli: (*a*) the secant stiffness modulus at 50% of the peak deviatoric stress in a standard drained triaxial test, E_{50}; (*b*) the one-dimensional compression tangent modulus, E_{oed}; and (*c*) the unloading–reloading modulus, E_{ur}. They are obtained using the following equations

$$E_{50} = E_{50}^{ref}\left(\frac{\sigma'_3}{p_{ref}}\right)^m \quad (7a)$$

$$E_{oed} = E_{oed}^{ref}\left(\frac{\sigma'_1}{p_{ref}}\right)^m \quad (7b)$$

$$E_{ur} = E_{ur}^{ref}\left(\frac{\sigma'_3}{p_{ref}}\right)^m \quad (7c)$$

where E_{50}^{ref}, E_{oed}^{ref} and E_{ur}^{ref} are the values at the reference confining stress level (see Table 3); σ'_1 and σ'_3 are the principal confining stresses; and m is a power that defines the stress-level dependency of the stiffness. The reference values for the stresses were taken from Benz (2006) for loose ($D_R = 20$–35%) and dense sand ($D_R = 72$–84%), based on drained triaxial and biaxial tests on Hostun sand. For the intermediate value of relative density, a linear interpolation was used. Table 3 shows the set of model parameters adopted in this paper.

Table 3. Constitutive parameters values used in the HSsmall model for the soil

Parameter	Symbol	Units	1*g*			40*g*
			$D_R = 20\%$	$D_R = 52\%$	$D_R = 88\%$	$D_R = 87{\cdot}5\%$
Cohesion	c	kPa	0	0	0	0
Angle of internal friction (peak)	ϕ'_p	degrees	34	49·6	55·1	49·8
Angle of dilatancy	ψ_{max}	degrees	0	20·6	28·8	20·8
Secant stiffness in standard drained triaxial test	E_{50}^{ref}	kPa	12 000	21 470	30 000	30 000
Tangent stiffness for primary oedometer loading	E_{oed}^{ref}	kPa	16 000	23 360	30 000	30 000
Unloading/reloading stiffness	E_{ur}^{ref}	kPa	60 000	75 780	90 000	90 000
Shear stiffness modulus	G_0^{ref}	kPa	81 500	88 650	138 000	138 000
Power for stress-level dependency of stiffness	m	—	0·75	0·55	0·55	0·55
Poisson's ratio for unloading–reloading	v_{ur}	—	0·25	0·25	0·25	0·25
Reference stress for stiffness	p'_{ref}	kPa	100	100	100	100
k_0 value for normal consolidation	k_0^{nc}	—	0·44	0·44	0·40	0·40
Shear strain level at which $G_s/G_0 \approx 0{\cdot}7$	$\gamma_{0\cdot7}$	—	0·000022	0·000034	0·00004	0·0002

Model at large confining stresses

The soil model's parameters chosen for the analyses at large confining stresses are the same as for the same relative density at low confining stresses (Table 3), with the exception of $\psi = 20{\cdot}8°$, $\phi'_p = 49{\cdot}8°$ and $\gamma_{0\cdot7} = 0{\cdot}0002$, modified to account for the different stress level at the trapdoor depth.

Cable model

Strain transfer within the cable could potentially be affected by the composite structure of the cable and a lack of shear transfer between each composite layer (i.e. buffer, cladding and glass core), which all have different mechanical properties. Ansari & Libo (1998) have shown that the internal structure of some fibre-optic cables can influence the strain reading by 30–50% of its real value if the gauge length is shorter than 60 mm. For longer gauge length, the attenuation maybe be reduced by a factor of 10%. This research applied to Michelson interferometric sensors, which are different cables from the cable selected for this study, with high internal shear transfer loss. The cable used for this research was calibrated by uniaxial tensile tests at different strain levels, showing very minimal loss caused by internal shear transfer (Kechavarzi *et al*., 2016). Consequently, this phenomenon was ignored in modelling going forward, and efforts were concentrated on understanding the effects of shear strain loss at the soil–cable interface, an acknowledged key limitation of the use of DFOS for this type of application (Gutiérrez *et al*., 2019), and an even stronger limitation of the work from Möller *et al*. (2022) at 1*g* (Xu *et al*., 2022b). The 2 mm dia. DFOS cable was modelled as an embedded beam element (Sadek & Shahrour, 2004), with a three-noded line element that can cross a ten-noded tetrahedral element meshing the soil. A built-in interface element was used to model the cable surface properties to best represent the soil–cable interaction. The beam element was assumed as an indefinitely elastic element, with an equivalent elastic modulus of $E = 200$ MPa. The embedded interface was elastic–perfectly plastic. The elastic stiffness of the element is assigned not to alter the elastic response of the cable–soil system, while the plastic behaviour is attained when a limiting shear force acts along the element skin, t_s, that is defined per unit length of the cable, according to equation (8)

$$|t_s| = \sigma_n^{avg} R_{inter} \tan\phi' \pi D \tag{8}$$

where σ_n^{avg} is the average soil normal stress on the cable skin surface evaluated at each step during the analysis; ϕ' is the soil's mobilised angle of friction; and D is the cable diameter. This means that the embedded beam interface reaches failure when the soil reaches its maximum shear stress (i.e. when the mobilised angle of friction is equal to the peak angle of friction $\phi' = \phi'_p$). R_{inter} is a strength reduction factor that allows the modelling of a 'smooth' interface ($R_{inter} = 0{\cdot}01$) or a 'rough' interface ($R_{inter} = 1$). The latter behaviour is used to approximate the cable behaviour when coated with glued sand. The embedded beam elements were fully fixed at the lateral boundaries of the model, far from the trapdoor, although such a level of constraint may not have developed in the tests at low relative densities, and was only observed at higher relative densities (Möller *et al*., 2022). This modelling choice was used to verify that this boundary constraint does not affect the cable deformation in the proximity of the trapdoor.

COMPARISON BETWEEN NUMERICAL RESULTS AND EXPERIMENTAL DATA

Validation

The numerical analyses were validated against the experimental measurements of soil deformation and fibre-optic strain profiles for small trapdoor displacements, representative of the 'early' formation of the sinkhole, and equal to a trapdoor displacement of 1–2% of its width (i.e. $\delta = 1$–2 mm). Any deformation beyond $\delta = 2$ mm is numerically costly and not immediately relevant to early warning and hence was not considered here.

For consistency with the procedure adopted in the experiments (Möller *et al*., 2022), the strain profiles for the soil and the modelled cable were obtained according to equations 9(a)–9(c), and schematised in Fig. 3

$$\varepsilon_{u,tot} = \frac{\sqrt{\left(\Delta X_i + u_{x,i+1} - u_{x,i}\right)^2 + \left(u_{y,i+1} - u_{y,i}\right)^2}}{\Delta X_i} - 1 \tag{9a}$$

$$\varepsilon_{u,y} = \frac{\sqrt{\left(\Delta X_i\right)^2 + \left(u_{y,i+1} - u_{y,i}\right)^2}}{\Delta X_i} - 1 \tag{9b}$$

$$\varepsilon_{u,x} = \frac{u_{x,i+1} - u_{x,i}}{\Delta X_i} \tag{9c}$$

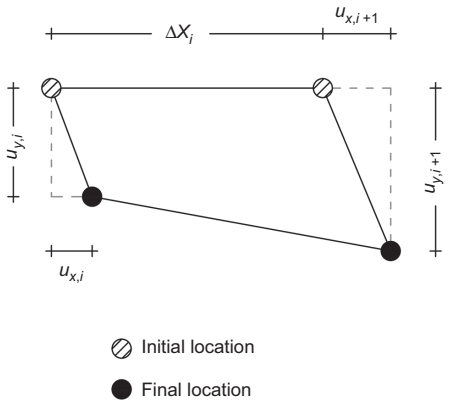

Fig. 3. Geometry for strain calculation

Equation (9a) evaluates the strains induced by both vertical and horizontal movements, while equations (9b) and (9c) identify the strains induced by vertical and horizontal movements, respectively.

The measured soil strain from test $D_R = 20\%$ evaluated with equation (9) are shown in Fig. 4; the scatter points are the raw experimental results from PIV data processing. These data have been interpolated (black line) using a modified Gaussian for vertical movements (Möller *et al.*, 2022) and a double standard Gaussian for horizontal movements for clarity, according to

$$S_h = a \times e^{-[(x-b)/c]^2} - a \times e^{-[(x+b)/c]^2} \quad (10)$$

where S_h is the horizontal soil displacement; x is the distance from the centreline; and a, b and c are fitting parameters. Figure 4 shows a comparison of the experimental soil strain profiles with the corresponding numerical results. The convention chosen in the figures is such that a dashed line represents the experimental results from Möller *et al.* (2022), while a solid line represents the numerical data from the present paper. The shape and magnitude of the strain profile between the experimental and numerical results shows good agreement, particularly for strains induced by vertical movement. For the strains induced by horizontal movement, the general shape is similar, although the magnitudes of the numerical results are approximately half the experimental results. The y-axes show that the strain induced by the vertical soil movements are more than one order of magnitude lower compared to those induced by horizontal movements. Horizontal movements induced by the trapdoor vertical movement thus played a major role in the measured horizontal strain profile.

The numerical strain profiles computed from cable movements using equation (9) are plotted in Fig. 5 and compared with the experimental data, directly measured by the Luna analyser. The advantage of the numerical analysis is the ability to separate the horizontal and vertical movements, which is not possible experimentally. The results are consistent with what has been observed for the soil strains: the comparison shows that for higher relative densities (i.e. $D_R = 88\%$) and small trapdoor displacements (i.e. $\delta = 1$ mm), strains within the cable far above the trapdoor (i.e. $z = 150$ mm) are induced by horizontal movements only. DFOS cables are therefore enabling an early detection of the vertical trapdoor displacement.

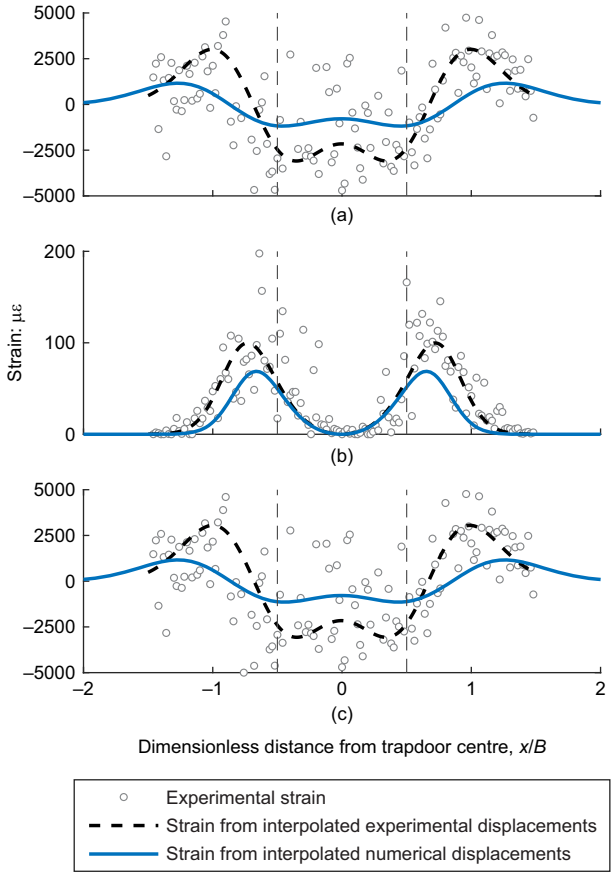

Fig. 4. Comparison between soil strains induced by (a) horizontal, (b) vertical and (c) total displacement in the 1g experimental results and numerical analysis of the laboratory test, far from the cables ($D_R = 20\%$, $\delta = 1$ mm, $z = 150$ mm)

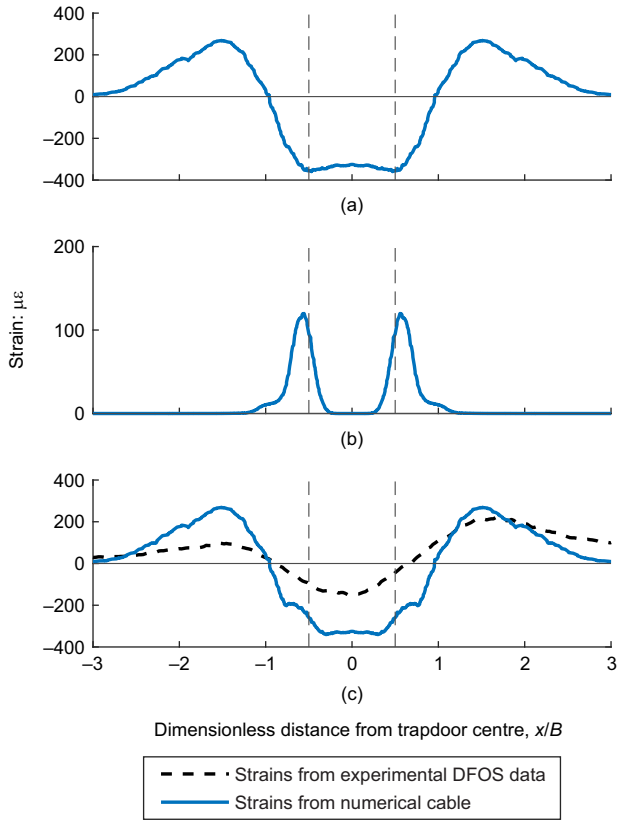

Fig. 5. Comparison between cable strains induced by (a) horizontal, (b) vertical and (c) total displacements in the 1g experimental results and numerical analysis of the laboratory test ($D_R = 20\%$, $\delta = 1$ mm, $z = 150$ mm, rough cable)

The horizontal strain profile induced in the soil and in the cable by horizontal movements (the contribution of vertical strains is negligible in comparison to the horizontal strains) is shown in Fig. 6 and Fig. 7, respectively, for a trapdoor displacement of $\delta = 1$ mm, for three different relative densities of soil and at three different distances above the trapdoor level. The comparison between experimental and numerical soil strains in Fig. 6 shows a good agreement in terms of strain magnitude, with both results indicating that the magnitude reduces with increasing relative densities and distance from trapdoor level. This also provides a good validation of the soil model employed here for low confining stresses.

Figure 7 shows a reasonable agreement between the profile and magnitude of the numerical and experimental cable strain for all distances from the trapdoor and all relative densities. This confirms the significant difference in strain magnitude between the cable and the soil noted by Möller *et al.* (2022), where it was observed that DFOS cable strain was approximately an order of magnitude lower than the corresponding soil strain determined from PIV. In particular, the shape, location of the peaks and magnitude matches well. This provides confidence that the model can be used to further analyse and understand the experimental tests performed by Möller *et al.* (2022), and potentially shed some light on the soil–cable interface to further explain this difference in strain magnitude.

Figure 8 shows shear strain along the model, on a vertical section centred at the cables' positions (rough cables), for $D_R = 88\%$ and $\delta = 1$ mm. Clearly there is a concentration of shear strain in proximity of the bottom cable's surface, and this concentration is located above the trapdoor edges, indicating that most of the shear transfer occurs in this area.

The soil–cable interface was investigated through modelling of two conditions: a smooth cable with $R_{inter} = 0{\cdot}01$, and a rough cable with $R_{inter} = 1$. Fig. 9 shows horizontal and vertical movements, respectively, of a smooth cable and a rough cable for $D_R = 52\%$ and $\delta = 1$ mm. The results show that the interface only has an effect on horizontal displacements, and does not affect vertical displacements. This indicates that for a smooth cable one should expect very small strains, since horizontal movements are the ones that induce most of the deformation (e.g. Fig. 5). Analysis of the numerical model, and more specifically of the soil strain field around the cable, shows that the simulated soil–rough cable interface permits a limited relative displacement between the soil and the cable (Fig. 10), allowing the reproduction of the experimental cable strain profiles. Therefore, the numerical results retrieve the difference of an order of magnitude observed experimentally between DFOS cable strains and PIV soil strains by Möller *et al.* (2022).

*Sinkhole prediction at 1***g**

As well as enabling the detection of a sinkhole as soon as it induces ground movements, fibre-optic cable data can be used to estimate the sinkhole size at depth and the extent of the surface damage zone at failure. Möller *et al.* (2022) show that the position of the maximum gradient (absolute value) in the fibre-optic strain profile provides a good estimate of the position of the trapdoor edges – that is, the size of the sinkhole. This methodology is applied here for further validation. First, the cable's strains are interpolated following Möller *et al.* (2022). This enables more accurate determination of the location of the maximum gradient, from which the distance between the inflection points, w_e, is derived. Fig. 11 illustrates the results for a trapdoor displacement of $\delta = 2$ mm, for the three different relative densities and at the three elevations above the trapdoor (i.e. $z = 50$, 100, 150 mm). For clarity, the extent of the trapdoor width is shown in light grey. The accuracy in the assessment of the trapdoor size is shown in Fig. 12, with Ω_t defined following Möller *et al.* (2022)

$$\Omega_t = \frac{w_e}{B} \tag{11}$$

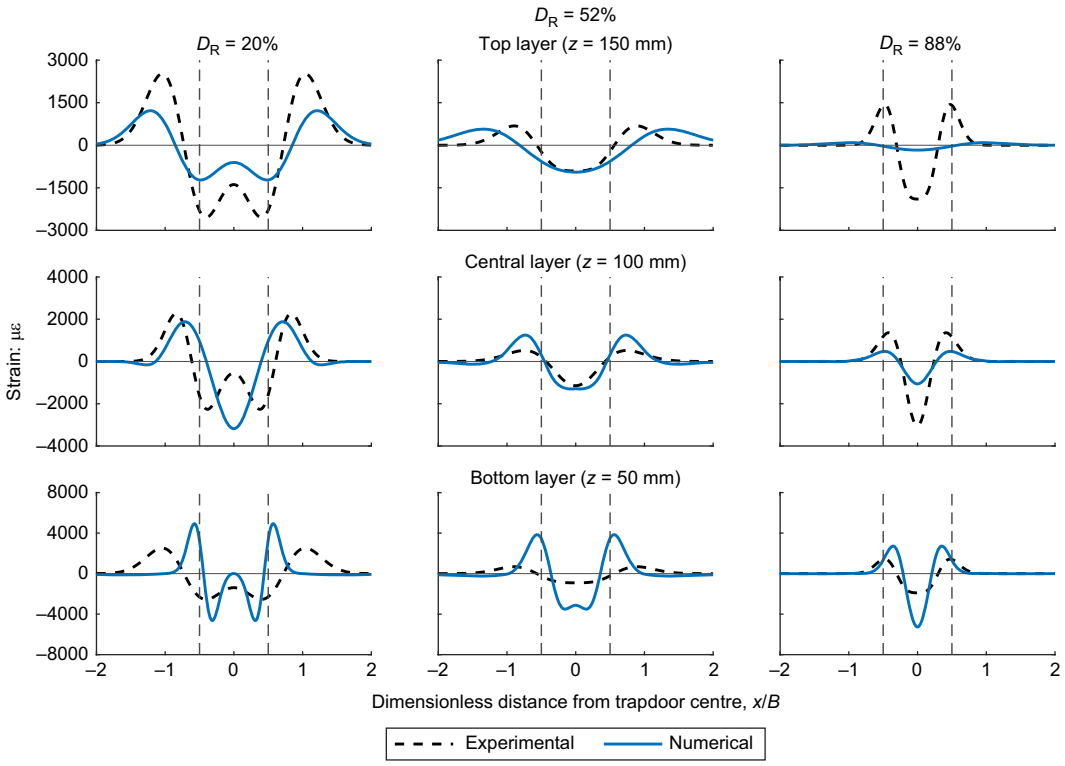

Fig. 6. Comparison between soil strains from horizontal movements at different densities and at three heights in the soil body in the 1*g* experimental results and numerical analysis of the laboratory test, far from the cables ($\delta = 1$ mm)

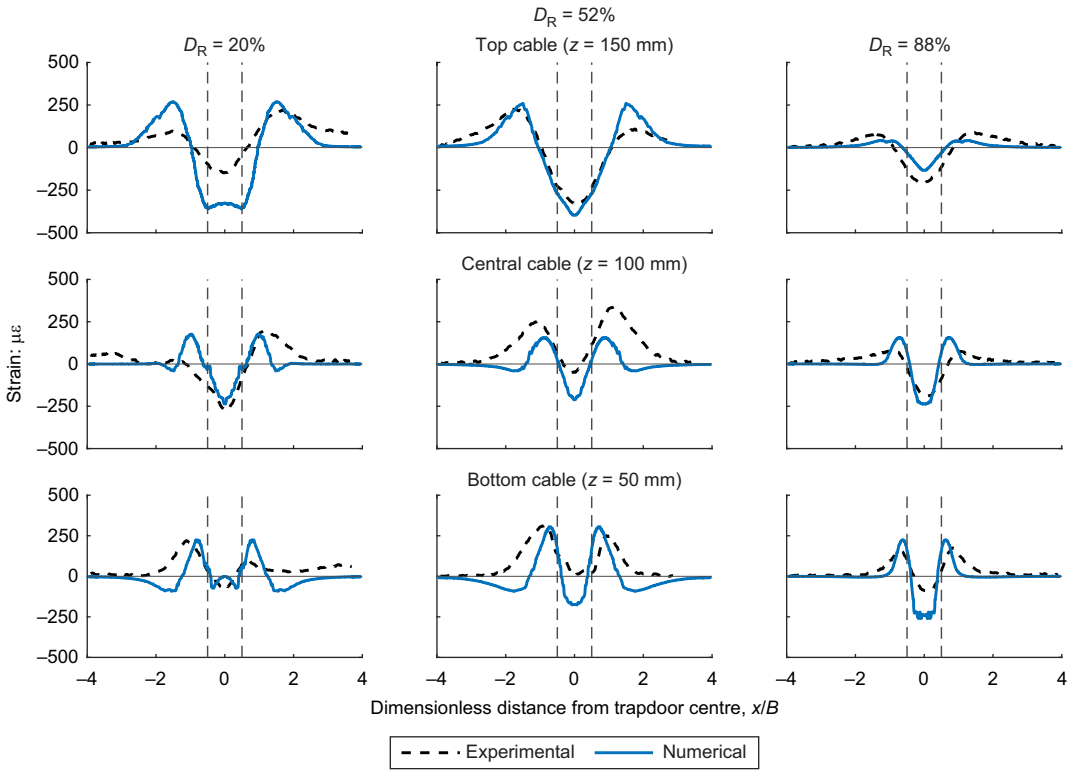

Fig. 7. Comparison between horizontal cable strains at different densities and at three heights in the soil body in the 1g experimental results and numerical analysis of the laboratory test, rough cables (δ = 1 mm)

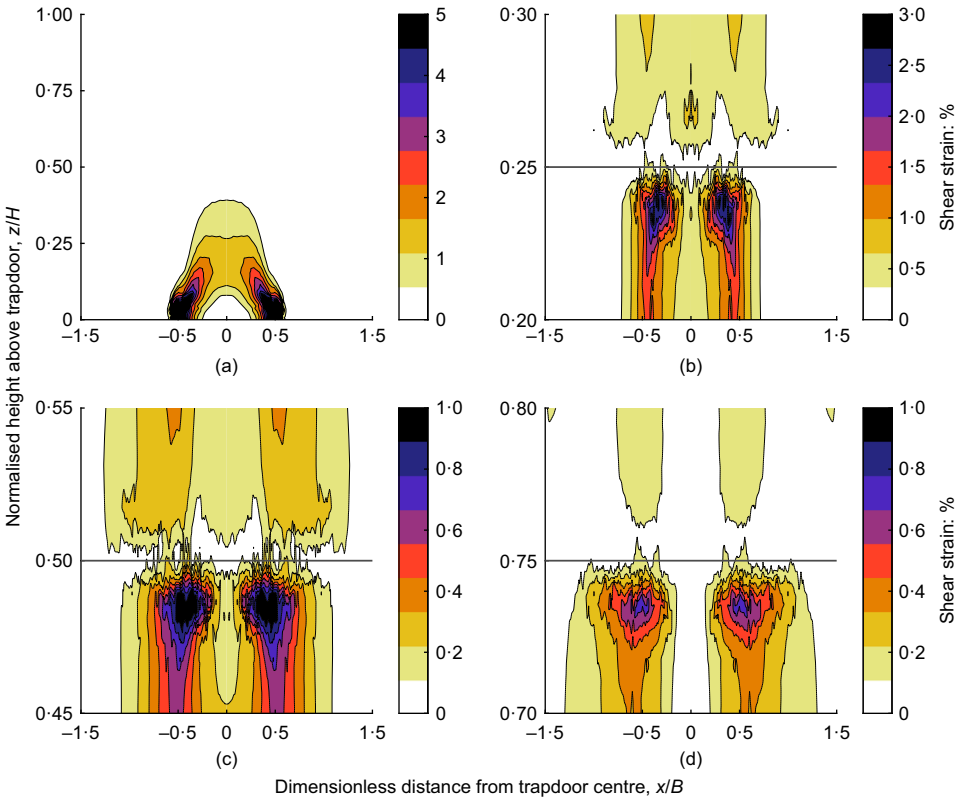

Fig. 8. Vertical section of numerical model (D_R = 88% and δ = 2 mm) representing shear strain: (a) far-field shear strain; (b) shear strain near the bottom cable; (c) shear strain near the central cable; (d) shear strain near the top cable

A value of Ω_t close to 1 reflects a close estimation of the trapdoor size from the cable strain profile. This shows that this method reasonably estimates the trapdoor width, with similar results obtained for smaller trapdoor displacement (δ = 1 mm). The data are also in good agreement with the experimental trends from Möller *et al.* (2022), exhibiting

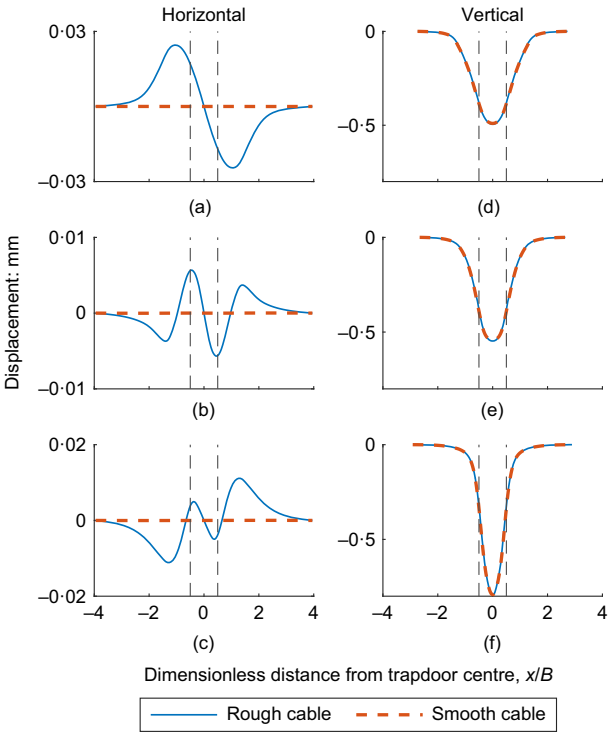

Fig. 9. Horizontal and vertical displacement of numerical cables for $D_R = 52\%$ and $\delta = 1$ mm, comparison between rough and smooth cables. (a), (d) Top cable; (b), (e) central cable; (c), (f) bottom cable

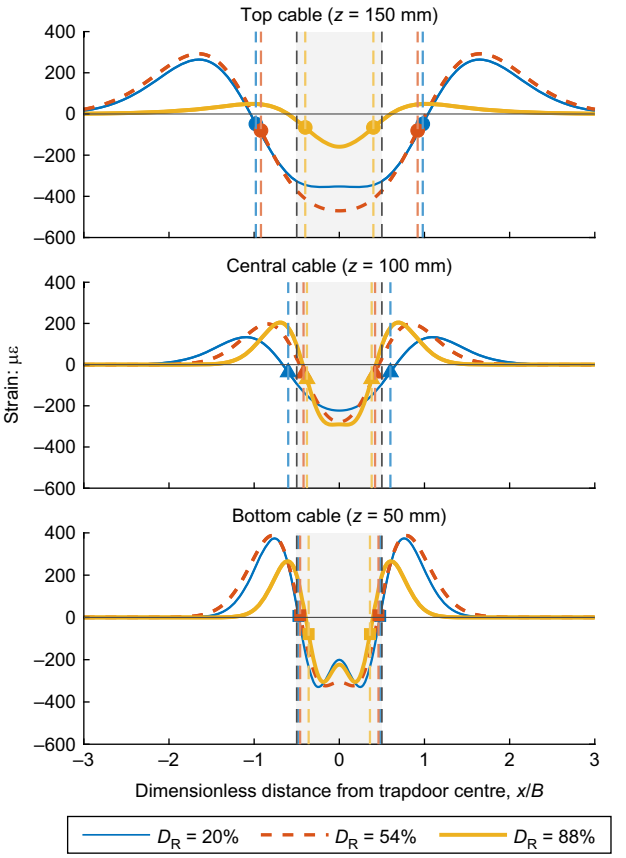

Fig. 11. Maximum gradient position from cable strain in the numerical analysis of the laboratory test ($\delta = 2$ mm)

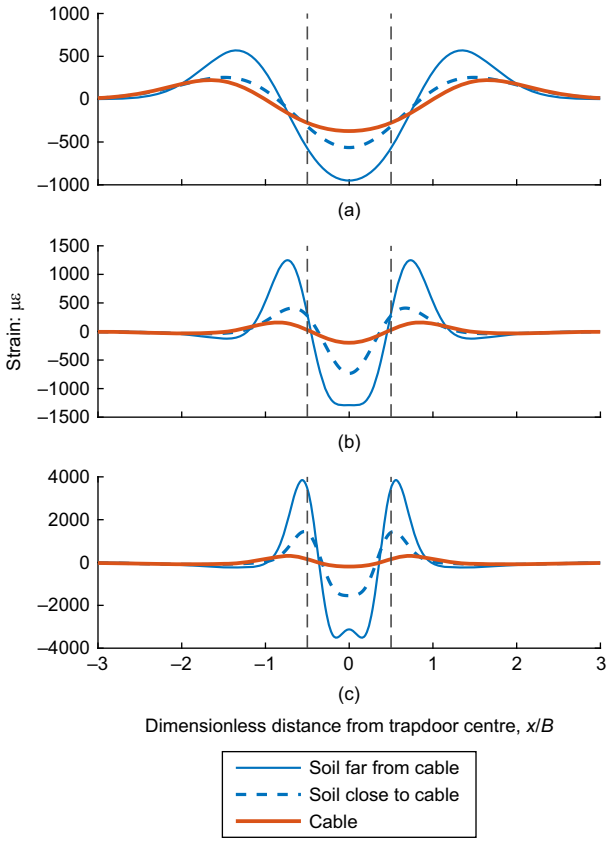

Fig. 10. Strain induced by horizontal movements for $D_R = 52\%$ and $\delta = 1$ mm, comparison between soil's strain (far from and close to the cable) and the rough cable for: (a) top layer and top cable; (b) central layer and central cable; (c) bottom layer and bottom cable

a very similar trend with both cable height and relative density.

The experimental results offer a more conservative estimate of the trapdoor width, which can be explained by the pinning conditions and the limited sample length adopted in the experiment. This experimental constraint induces a wider trough of the fibre-optic cable strain profile compared to that expected from numerical analyses, a limitation that requires further exploration in the future. Nevertheless, the results from the numerical analyses show that the top cable is able to provide a conservative estimate of the sinkhole size for loose to medium dense sand. For the other cases, using the maximum gradient may lead to an under-prediction of the sinkhole size, and the method proposed by Möller *et al.* (2022) might need to be adjusted.

LARGE-SCALE APPLICATION

Validation

Despite providing valuable insight regarding the DFOS behaviour, the low stress level in the experiments conducted by Möller *et al.* (2022) is actually one of the key limitations of the work. Although careful consideration was given to the scaling laws, the results cannot be used to directly predict the behaviour at full scale, in particular the quantitative response. For this, tests at enhanced gravity in the centrifuge would be needed; however, as mentioned by Möller *et al.* (2022) and Eichhorn (2021), it is not currently possible to use the fibre-optic analyser needed in the geotechnical centrifuge. To verify the robustness of the methodology outlined above for early warning detection of sinkhole formation at realistic stress levels, a 3D FE model of the centrifuge test from da Silva (2017) was performed, adding embedded fibre-optic cables for analyses.

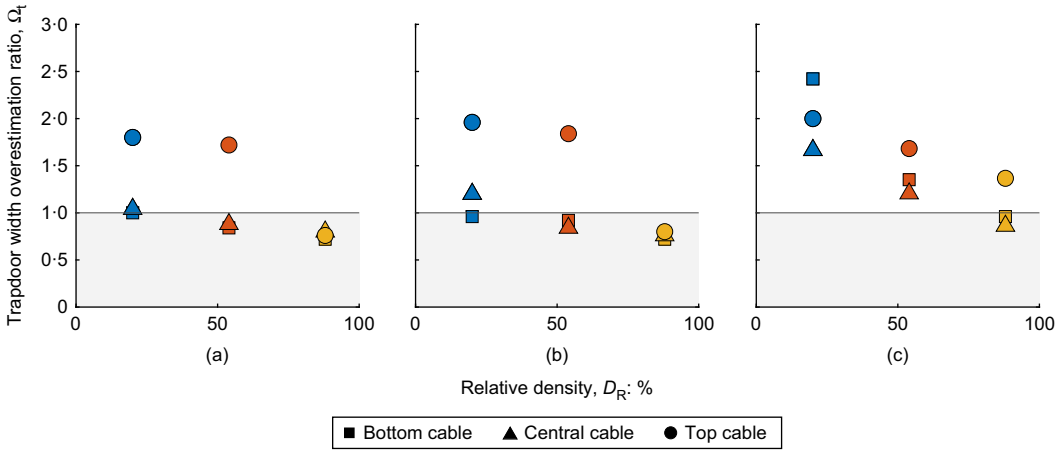

Fig. 12. Trapdoor size prediction from cable's strain data: (a) numerical δ = 1 mm; (b) numerical δ = 2 mm; (c) experimental δ = 2 mm (modified after Möller *et al.* (2022)); the different shades of the symbols are to facilitate comparison of the relative densities with Fig. 11

The numerical model was created at prototype scale, reproducing the formation of a 2 m wide sinkhole (i.e. trapdoor width) in plane-strain conditions, located 4 m below the ground level in a cohesionless sand at $D_R = 87{\cdot}5\%$. Using the framework established by Möller *et al.* (2022), the 'early' stage of the sinkhole formation corresponds to a trapdoor displacement of $\delta = 40$ mm – that is, 2% of the trapdoor width. The material model used is the HSSmall model, and its parameters are indicated in Table 3.

Figure 13 shows the comparison between the experimental and numerical ground surface settlement profiles. The shape of the ground settlement profile is well captured, with an overestimation of the magnitude of about 25%. This is because the material model does not enable a variation of dilation angle within the model and a constant dilation angle had to be used, evaluated here at the trapdoor level. In the centrifuge model, however, this dilation angle reduces with overburden pressure, and therefore the numerical model has a lower dilatancy compared to the centrifuge test at the soil surface, which leads to larger settlements. However, this is sufficient here to have a good estimate of the expected sinkhole behaviour at realistic stress levels at the early stage of sinkhole formation.

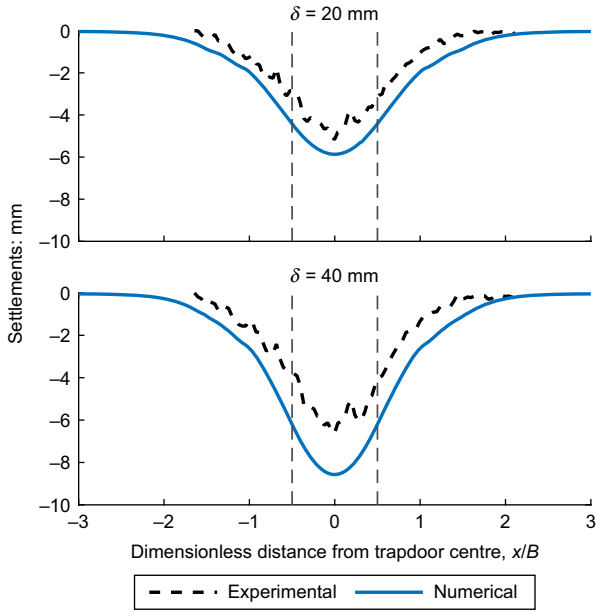

Fig. 13. Comparison between centrifuge experimental and numerical surface soil settlement profiles

Early warning of sinkhole formation

Figure 14 shows the cable strain profiles obtained for this model, as well as the strain caused by horizontal and vertical movements. Fig. 14 only displays the results for the top cable, as it is the location of practical interest for this study.

The cases of rough and smooth cables are considered, showing similar results to those observed previously for the 1g tests for the rough cable. Horizontal displacements are governing the strains within the cable (compare Fig. 5 with Fig. 14). This figure also shows that the strains generated by the horizontal movements are not equal to zero for the smooth cable, confirming that at higher confining stresses, enhanced coupling between the soil and the cable enables the cable to move horizontally with the soil better.

However, the inflection points used to estimate the size of the sinkhole (equation (11)) are considerably closer to the centre of the trapdoor for the smooth cable and lead to large underestimations. This is shown in Fig. 15, where the results for the rough cable display satisfactory estimation for the top cable only. The predicted trapdoor width would be $w_e = 2{\cdot}04 - 1{\cdot}82$ m (to be compared with $B = 2$ m) for $\delta = 40$ mm for this specific case, but is significantly smaller for cables located at greater depth and/or when full coupling of the soil–cable interface is not achieved. This result shows that further experimental work at higher stress levels is needed to validate further the method outlined by Möller *et al.* (2022).

The results also show relatively good agreement with the 1g test obtained for $D_R = 52\%$ (see Fig. 12), which corresponds to a relative density of $D_R = 87{\cdot}5\%$ at 40g (see Möller *et al.* (2022) for details on the scaling laws). This gives some level of confidence in the use of the 1g tests to pursue this investigation further, provided that further work on boundary conditions is performed to reduce the artificial tension in the cable caused by boundary conditions.

The results from the 3D FE analyses at both 1g and 40g, as well as the experimental data, demonstrate the importance of the horizontal soil movements in the ability of the DFOS to identify the presence of an active subsidence at depth. These results concur with previous research (e.g. Carbonel *et al.*, 2014; Kim *et al.*, 2016; Gutiérrez *et al.*, 2018, 2012), in which large horizontal movement of the ground towards the centre of the sinkhole has also been observed for sagging subsidence. However, the prominence of the horizontal strain over the vertical strain had not been made clear to date (Gutiérrez *et al.*, 2019).

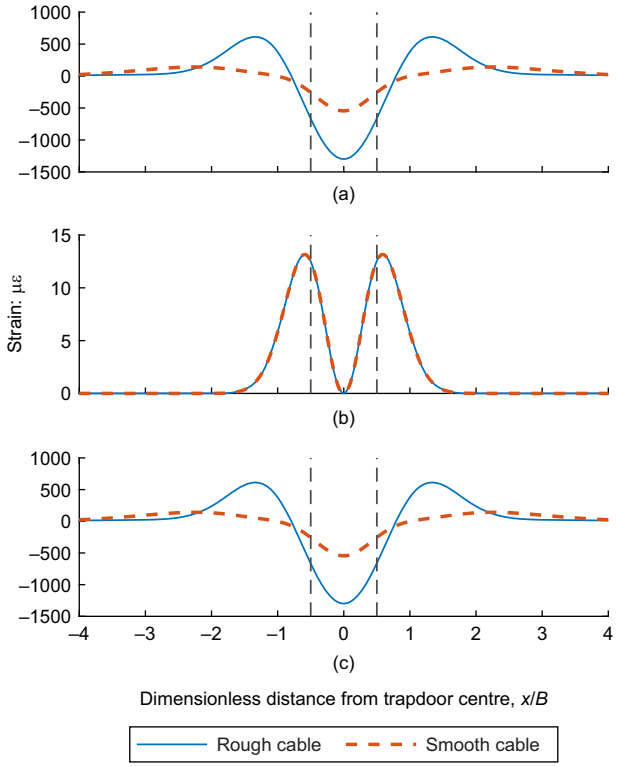

Fig. 14. Comparison between rough and smooth cable, top cable $\delta = 40$ mm: (a) strains induced by horizontal displacements; (b) strains induced by vertical settlements; (c) total strains induced by horizontal and vertical displacements

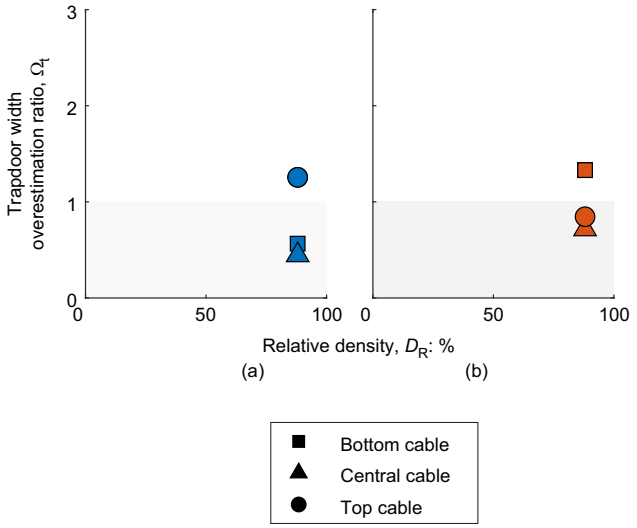

Fig. 15. Trapdoor size prediction from numerical cable's strain, for $\delta = 40$ mm: (a) rough cable; (b) smooth cable; the different shades of the symbols are to facilitate comparison of the relative densities with Fig. 14

Finally, these results indicate that the better the soil–cable coupling, the more precise the results, because the cable is then more able to deform horizontally with the soil. These results confirm that improving the soil–cable coupling increases the ability of the cable to deform horizontally with the soil. Therefore, it is important to use in practice elements that can be horizontally deployed and have higher surface area, in order to increase the amount of shear transferred at the interface. This would, however, constrain the cable horizontally and therefore prevent this movement. The results shown here seem therefore to indicate that this laying technique would need to be adapted. Nevertheless, the results demonstrate the viability of the use of DFOS as an early warning at realistic stress levels if the cables are sufficiently well coupled with the soil, and laid within a narrow geogrid or bare.

Extension to 3D cable laying

One of the other key limitations of the work presented above is the 2D nature of the plane-strain conditions, which naturally enforces the cable to be directly above the centre of the trapdoor/subsidence. There is a large uncertainty as to what would happen in the case where the cable is located eccentrically compared with the centre of the sinkhole, or even outside the trapdoor/sinkhole width. With this purpose, the calibrated numerical model described in the previous section was extended to a 3D circular sinkhole, as shown in Fig. 16. A series of cables were placed immediately above the trapdoor centre ($y/D = 0$) for comparison with the 2D experiments, and then at $y/D = 0{\cdot}25$ eccentrically from the centre, at $y/D = 0{\cdot}50$ on the edge of the trapdoor, and at $y/D = 0{\cdot}75$, $1{\cdot}00$, $1{\cdot}50$ and $2{\cdot}00$ outside the trapdoor.

The strains recorded within the cables for $\delta = 40$ mm are shown in Fig. 17. In this series of plots, the strain profiles from the bottom cable for $y/D = 1{\cdot}00$, $1{\cdot}50$ and $2{\cdot}00$ (Figs 17(f), 17(g) and 17(h)) are practically zero, with

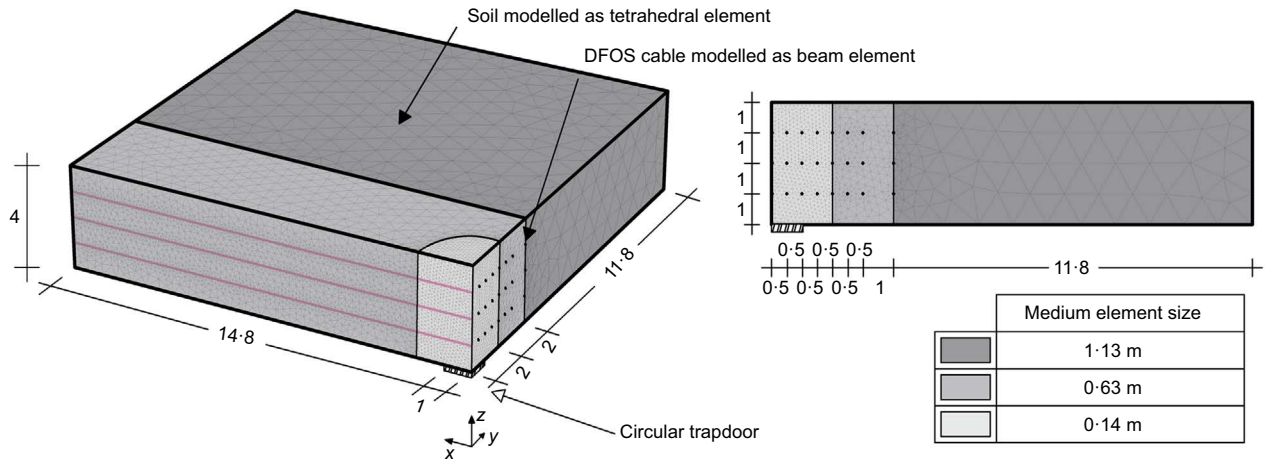

Fig. 16. Plaxis 3D numerical model representing a quarter of the axisymmetric problem with soil modelled as tetrahedral element and fibre-optic cable modelled as an embedded beam element (15·8 × 15·8 × 4 m). Dimensions in m

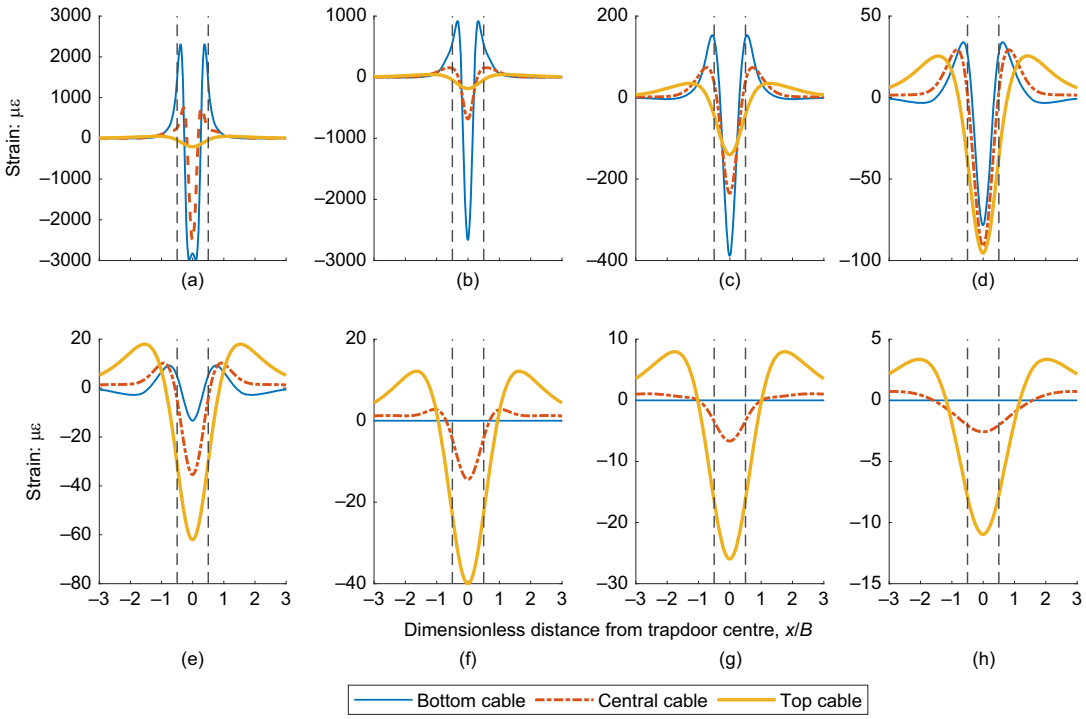

Fig. 17. Horizontal strain profiles within the cable in axial symmetric conditions for $\delta = 40$ mm: (a) $y/D = 0$; (b) $y/D = 0{\cdot}25$; (c) $y/D = 0{\cdot}50$; (d) $y/D = 0{\cdot}75$; (e) $y/D = 1{\cdot}00$; (f) $y/D = 1{\cdot}25$; (g) $y/D = 1{\cdot}50$; (h) $y/D = 2{\cdot}00$

very low magnitude of less than 1 microstrain. Therefore a 0 horizontal line was used for clarity. The results show a clear drop of strain magnitude at $y/D = 0{\cdot}50$, and an even larger drop for $y/D \geq 0{\cdot}75$, which might not be measurable in practice.

The results also illustrate that cables located close to the soil surface, but away from the immediate zone above the sinkhole formation, benefit from the funnel shape of the deformation mechanism. Clearly, if the cable is located anywhere directly above the trapdoor (here, $y/D = 0{\cdot}00$, $0{\cdot}25$, $0{\cdot}50$, $0{\cdot}75$), the lower the cable is, the more clearly it senses the displacement induced by the trapdoor. However, cables located horizontally away from the trapdoor footprint ($y/D \geq 0{\cdot}75$) will be able to sense ground deformation when placed relatively close to the soil surface if they are within the funnel mechanism generated by the sinkhole expansion, and therefore are deformed by the horizontal soil movement within that zone.

CONCLUSIONS

The use of DFOS to detect the onset of sinkhole formation at an early stage can help prevent damage induced in infrastructures built within the surface damaged zone at full collapse. This paper uses 3D FEAs to expand the experimental evidence on the feasibility of using this technology. The numerical analyses have been validated against experimental results from 1$\boldsymbol{g}$ trapdoor tests on DFOS cables embedded in a cohesionless soil layer. The displacement and strain fields measured in the tests were correctly predicted by carefully calibrating the constitutive model at small strain and stress levels. A method for numerical modelling of Hostun sand at low confining stresses is discussed and a list of calibrated parameters is provided. A frictional contact between the cable and the soil was defined in the numerical model to closely mimic the soil–cable interface during experimental testing. The 3D FE model enables inspection of the soil strain field around the cable and in the far field. This makes it possible to gain information on the reciprocal influence of the cable and the soil, which may affect the cable strain.

Experimental evidence has shown that measured fibre-optic cable strains were much lower than PIV-measured soil strains. The 3D numerical analyses corroborate this experimental observation, showing that the soil–cable interface permits a limited relative displacement between the soil and the cable. The difference between PIV measured soil strains and DFOS cable strain is hence mostly due to a loss of shear transfer between the soil and the cable interface.

The numerical results also show that the strains within the cable are mostly induced by horizontal movements. Hence, DFOS cables horizontally deployed are potentially enabling the detection of the sinkhole-induced early vertical displacement. The FEAs confirmed common knowledge that enhanced measurement of the soil strain is obtained when improving the coupling between the soil and the cable. However, the research also highlights that the signature strain profile for cables located close to the soil surface is generated almost purely by horizontal strain within the ground, which is transferred to the cable provided that its horizontal movement is not constrained. This provides valuable information for cable-laying techniques, which is currently an important area of research (e.g. Sparrevik *et al.*, 2022; Xu *et al.*, 2022a). The results of this paper imply that the horizontal stiffness of the system used to enhance soil–cable coupling in practice must be reduced as much as possible.

The results of the numerical analyses also enabled validation of the methodology outlined by Möller *et al.* (2022) to locate the sinkhole and assess its size for realistic stress levels in the field. The limitations of the methodology used by Möller *et al.* (2022) are also highlighted, and in particular the cable installation at the boundary and the limited size of the box, a problem that would still persist in the centrifuge. Nevertheless, this paper provides confidence in the 1$\boldsymbol{g}$ testing method as a proof of concept for the use of DFOS cables above subsidence formation.

Finally, the analyses presented in this paper enable the findings to be extended numerically to the formation of sinkholes in three dimensions. The results show that DFOS would display a large signature strain profile if located anywhere within $0{\cdot}5D$ of the sinkhole centreline, but display a much attenuated signal when located at or beyond $0{\cdot}75D$, where D is the sinkhole diameter. The results also demonstrate better accuracy for cables laid closer to the soil surface, where the horizontal ground movements are higher. This provides grounds for further research on how to lay fibre-optic cables to obtain efficient early warning, as well as on the interpretation of the strain to predict both the sinkhole size and surface damage zone. In particular, future research will explore the possibility of using a combination of cables instead of a single cable, laid into a series of lines or grids to enable more accurate sensing of the sinkhole location in the horizontal plane. The possibility of using combined differential interferometric synthetic aperture radar (DInSAR) technology will also be investigated for this purpose (Abadie *et al.*, 2023).

The reference tests used in this paper were evidently performed in controlled conditions, where the measurements were not affected by changes in strain from external factors. In situ applications will, however, be subjected to temperature and moisture content changes, as well as vibrations from human activities (train, road, construction, etc.), which will pollute the otherwise sensitive DFOS signal (Guan *et al.*, 2015). Temperature changes can typically be corrected by adding a fibre that senses seasonal and daily changes in temperature on a specific channel of the interrogator (Kechavarzi *et al.*, 2016), but this technique might not be sufficient at small strain levels, as needed for this particular application. Further work is required to identify how to filter the signal properly and reveal the signature strain profile indicating sinkhole formation for application of this type of technology in the field; however, this paper demonstrates that the use of distributed fibre-optic sensing for the detection of early stages of sinkhole formation at full scale is a promising technology.

ACKNOWLEDGEMENTS

The authors are grateful to CSIC (EPSRC (EP/N021614/1) and Innovate UK (920035)) for funding and supporting this work and Dr Jennifer Schooling and Professor Giulia Viggiani for facilitating the collaboration between the University of Naples Federico II and the University of Cambridge, which enabled Mr Gianluigi Della Ragione's internship at CSIC within the Erasmus + programme. The authors are also thankful to the Schofield Centre and its Director, Professor Gopal Madabhushi, for their support with the laboratory experiments. Fruitful advice and discussion with Professor Malcolm Bolton, Professor Sadik Oztoprak, Dr Sam Stanier and Professor Giulia Viggiani were also very valuable for the development of this project.

NOTATION

a	fitting parameter for equation (10)
B	trapdoor width
b	fitting parameter for equation (10)
c	cohesion or fitting parameter for equation (10)
D	cable diameter
D_R	relative density
E	Young's modulus of cable
E_{50}	secant stiffness modulus at 50% of the peak deviatoric stress in standard drained triaxial test
E_{oed}	one-dimensional tangent stiffness modulus in oedometric compression test
E_{ur}	unloading–reloading stiffness modulus
e	void ratio or Euler number
G	shear stiffness
G_0	initial shear stiffness
$\boldsymbol{g}$	acceleration of gravity
H	soil specimen height
I_R	dilatancy index
m	power coefficient for stress-level dependency of stiffness
p'	effective confinement stress
p_{atm}	atmospheric pressure (assumed equal to 100 kPa)
p_{ref}	reference confining pressure
Q	fitting parameter for equation (2)
R	fitting parameter for equation (2)
S_h	horizontal soil displacement
t_s	shear force at the cable skin per unit length
u_x	horizontal movement
u_y	vertical movement
w_e	trapdoor width estimated through numerical cable strain profile
x	distance from the trapdoor centreline
z	distance from the trapdoor level
$\gamma_{0{\cdot}7}$	shear strain level at which $G/G_0 \approx 0{\cdot}7$
δ	trapdoor displacement
$\varepsilon_{u,tot}$	cable axial strain induced by both vertical and horizontal movements
$\varepsilon_{u,x}$	cable axial strain induced by horizontal movements only
$\varepsilon_{u,y}$	cable axial strain induced by vertical movements only
σ'_1	maximum principal effective stress
σ'_3	minimum principal effective stress
σ_n^{avg}	average soil normal stress on the cable skin surface
ϕ'	mobilised angle of friction
ϕ'_c	critical angle of friction
ϕ'_p	peak angle of friction
ψ	dilatancy angle
Ω_t	trapdoor width overestimation ratio

REFERENCES

Abadie, C. N., da Silva Burke, T. S., Xu, X., Della Ragione, G., Möller, T., Selvakumaran, S. & Bilotta, E. (2023). SINEW: SINkhole early warning. *2nd international conference on construction resources for environmentally sustainable technologies (CREST)*, Fukuoka, Japan.

Ansari, F. & Libo, Y. (1998). Mechanics of bond and interface shear transfer in optical fiber sensors. *J. Engng Mech.* **124**, No. 4, 385–394.

Belli, R., Glisic, B., Inaudi, D. & Gebreselassie, B. (2009). Smart textiles for SHM of geostructures and buildings. *4th international conference on structural health monitoring on intelligent infrastructure (SHMII-4)*, Zurich, Switzerland, paper 368.

Benz, T. (2006). *Small-strain stiffness of soils and its numerical consequences*. PhD thesis, University of Stuttgart, Stuttgart, Germany.

Benz, T., Schwab, R. & Vermeer, P. (2009). Small strain stiffness in geotechnical analyses. *Bautechnik* **86**, No. 1, 16–27.

Blairon, S., Henault, J. M., Buchoud, E., Vinceslas, G. & Delepine-Lesoille, S. (2011). Truly distributed optical fiber extensometers for geotechnical structure monitoring (dikes and underground repository): influence of sensor external coating. *8th international symposium of field measurement in geomechanics*, Berlin, Germany.

Bolton, M. D. (1986). The strength and dilatancy of sands. *Géotechnique* **36**, No. 1, 65–78, https://doi.org/10.1680/geot.1986.36.1.65.

Brady, H. G. & Brown, E. T. (1993). *Rock mechanics for underground mining*. London, UK: Chapman and Hall.

Brinkgreve, R. B. J., Engin, E. & Swolfs, W. M. (2015). *Plaxis 3D 2015 manual*. Delft, the Netherlands: Plaxis bv, Bentley Systems, Inc.

Buchoud, E., Vrabie, V., Mars, J. I., D'Urso, G., Girard, A., Blairon, S. & Hénault, J. M. (2016). Quantification of submillimeter displacements by distributed optical fiber sensors. *IEEE Trans. Instrum. Meas.* **65**, No. 2, 413–422.

Carbonel, D., Rodríguez, V., Gutiérrez, F., Mccalpin, J. P., Linares, R., Roqué, C., Zarroca, M., Guerrero, J. & Sasowsky, I. (2014). Evaluation of trenching, ground penetrating

radar (GPR) and electrical resistivity tomography (ERT) for sinkhole characterization. *Earth Surf. Process. Landforms* **39**, No. 2, 214–227.

Chakraborty, T. & Salgado, R. (2010). Dilatancy and shear strength of sand at low confining pressures. *J. Geotech. Geoenviron. Engng* **136**, No. 3, 527–532.

Chang, L. & Hanssen, R. F. (2014). Detection of cavity migration and sinkhole risk using radar interferometric time series. *Remote Sens. Environ.* **147**, 56–64.

Cooper, A. H., Farrant, A. R. & Price, S. J. (2011). The use of karst geomorphology for planning, hazard avoidance and development in Great Britain. *Geomorphology* **134**, No. 1–2, 118–131.

Darendeli, M. B. & Stokoe, K. H. (2001). *Development of a new family of normalized modulus reduction and material damping curves*, Engineering Report GD01-1. Austin, TX, USA: University of Texas.

da Silva, T. S. (2017). *Centrifuge modelling of the behaviour of geosynthetic-reinforced soils above voids*. PhD thesis, University of Cambridge, Cambridge, UK.

da Silva Burke, T. S. & Elshafie, M. Z. E. B. (2021). Arching in granular soils: experimental observations of deformation mechanisms. *Géotechnique* **71**, No. 10, 866–878, https://doi.org/10.1680/jgeot.19.P.174.

Eichhorn, G. N. (2021). *Landslide–pipeline interaction in unsaturated silty slopes*. PhD thesis, University of Cambridge, Cambridge, UK.

Guan, Z., Jiang, X. Z. & Gao, M. (2013). A calibration test of karst collapse monitoring device by optical time domain reflectometry (BOTDR) technique. In *National Cave and Karst Research Institute symposium 2: proceedings of the 13th multidisciplinary conference on sinkholes and the engineering and environmental impacts of karst* (eds L. Land, D. H. Doctor and J. B. Stephenson), pp. 71–77. Carlsbad, NM, USA: National Cave and Karst Research Institute.

Guan, Z., Jiang, X. Z., Wu, Y. B. & Pang, Z. Y. (2015). Study on monitoring and early warning of karst collapse based on BOTDR technique. In *Proceedings of the 14th multidisciplinary conference on sinkholes and the engineering and environmental impacts of karst (NCKRI symposium 5)* (eds D. H. Doctor, L. Land and J. B. Stephenson), pp. 407–414. Carlsbad, NM, USA: National Cave and Karst Research Institute.

Gutiérrez, F., Carbonel, D., Guerrero, J., McCalpin, J. P., Linares, R., Roqué, C. & Zarroca, M. (2012). Late Holocene episodic displacement on fault scarps related to interstratal dissolution of evaporites (Teruel Neogene Graben, NE Spain). *J. Struct. Geol.* **34**, 2–19.

Gutiérrez, F., Zarroca, M., Linares, R., Roqué, C., Carbonel, D., Guerrero, J., McCalpin, J. P., Comas, X. & Cooper, A. H. (2018). Identifying the boundaries of sinkholes and subsidence areas via trenching and establishing setback distances. *Engng Geol.* **233**, 255–268.

Gutiérrez, F., Benito-Calvo, A., Carbonel, D., Desir, G., Sevil, J., Guerrero, J., Martínez-Fernández, A., Karamplaglidis, T., García-Arnay,Á. & Fabregat, I. (2019). Review on sinkhole monitoring and performance of remediation measures by high-precision levelling and terrestrial laser scanner in the salt karst of the Ebro Valley, Spain. *Engng Geol.* **248**, 283–308.

Iglesia, G. R., Einstein, H. H. & Whitman, R. V. (2014). Investigation of soil arching with centrifuge tests. *J. Geotech. Geoenviron. Engng* **140**, No. 2, 04013005.

Inaudi, D. (2017). Sensing solutions for assessing the stability of levees, sinkholes and landslides. In *Sensor technologies for civil infrastructures. Volume 2: applications in structural health monitoring* (eds M. L. Wang, J. P. Lynch and H. Sohn), pp. 396–421. Cambridge, UK: Woodhead Publishing.

Jennings, J. E., Brink, A. B. A., Louw, A. & Gowan, G. D. (1965). Sinkholes and subsidence in the Transvaal dolomite of South Africa. *Proceedings on soil mechanics: 6th international conference*, Montreal, Canada.

Kechavarzi, C., Soga, K., de Battista, N., Pelecanos, L., Elshafie, M. Z. E. B. & Mair, R. J. (2016). *Distributed fibre optic strain sensing for monitoring civil infrastructure: a practical guide*. London, UK: ICE Publishing.

Kim, J. W., Lu, Z. & Degrandpre, K. (2016). Ongoing deformation of sinkholes in Wink, Texas, observed by time-series Sentinel-1A SAR interferometry (preliminary results). *Remote. Sens. (Basel)* **8**, No. 4, article 313, https://doi.org/10.3390/rs8040313.

Klar, A., Dromy, I. & Linker, R. (2014). Monitoring tunnelling induced ground displacements using distributed fiber-optic sensing. *Tunn. Undergr. Space Technol.* **40**, 141–150.

Lancelot, L., Shahrour, I. & Al Mahmoud, M. (2006). Failure and dilatancy properties of sand at relatively low stresses. *J. Engng Mech.* **132**, No. 12, 1396–1399.

Lanticq, V., Bourgeois, E., Magnien, P., Dieleman, L., Vinceslas, G., Sang, A. & Delepine-Lesoille, S. (2009). Soil-embedded optical fiber sensing cable interrogated by Brillouin optical time-domain reflectometry (B-OTDR) and optical frequency-domain reflectometry (OFDR) for embedded cavity detection and sinkhole warning system. *Meas. Sci. Technol.* **20**, No. 3, 034018.

Lee, E. J., Shin, S. Y., Ko, B. C. & Chang, C. (2016). Early sinkhole detection using a drone-based thermal camera and image processing. *Infrared Phys. Technol.* **78**, 223–232.

Luna Innovations (2020). *Optical distributed sensor interrogator model ODiSI 6100: data sheet*. Blacksburg, VA, USA: Luna Innovations Incorporated.

Möller, T., da Silva Burke, T. S., Xu, X., Della Ragione, G., Bilotta, E. & Abadie, C. N. (2022). Distributed fibre optic sensing for sinkhole early warning: experimental study. *Géotechnique*, https://doi.org/10.1680/jgeot.21.00154.

Oztoprak, S. & Bolton, M. D. (2011). Parameter calibration of a modified hyperbolic model for sands using pressuremeter test data. In *Deformation characteristics of geomaterials* (eds C.-K. Chung, H.-K. Kim, J.-S. Lee, Y.-H. Jung and D.-S. Kim), pp. 949–956. Amsterdam, the Netherlands: IOS Press.

Sadek, M. & Shahrour, I. (2004). A three dimensional embedded beam element for reinforced geomaterials. *Int. J. Numer. Analyt. Methods Geomech.* **28**, No. 9, 931–946.

Schanz, T. & Vermeer, P. A. (1996). Angles of friction and dilatancy of sand. *Géotechnique* **46**, No. 1, 145–151, https://doi.org/10.1680/geot.1996.46.1.145.

Schanz, T., Vermeer, P. A. & Bonnier, P. G. (1999). The hardening soil model: formulation and verification. In *Beyond 2000 in computation geotechnics* (ed. R. B. J. Brinkgreve), pp. 281–290. Rotterdam, Netherlands: Balkema.

Sparrevik, P., Meland, H. J. & Joonsang, P. (2022). Distributed fibre optic ground deformation sensing. *11th international symposium on field monitoring in geomechanics (ISFMG2022)*, London, UK.

Stanier, S. A., Blaber, J., Take, W. A. & White, D. J. (2016). Improved image-based deformation measurement for geotechnical applications. *Can. Geotech. J.* **53**, No. 5, 727–739.

Taylor, R. N. (ed.) (1994). *Geotechnical centrifuge technology*, 1st edn. Abingdon, UK: Taylor & Francis.

Tran, K. T., McVay, M., Faraone, M. & Horhota, D. (2013). Sinkhole detection using 2D full seismic waveform tomography. *Geophysics* **78**, No. 5, R175–R183.

Van Schoor, M. (2002). Detection of sinkholes using 2D electrical resistivity imaging. *J. Appl. Geophys.* **50**, No. 4, 393–399.

Villard, P. & Briancon, L. (2008). Design of geosynthetic reinforcements for platforms subjected to localized sinkholes. *Can. Geotech. J.* **45**, No. 2, 196–209.

Wichtmann, T. & Triantafyllidis, T. (2004). Influence of a cyclic and dynamic loading history on dynamic properties of dry sand, part I: cyclic and dynamic torsional prestraining. *Soil Dyn. Earthq. Engng* **24**, No. 2, 127–147.

Xu, X., Kechavarzi, C., Wright, D., Horgan, G., Hangen, H., de Battista, N., Woods, D., Bertrand, E., Trinder, S. & Sartain, N. (2022a). Fibre optic instrumented geogrid for ground movement detection. *11th international symposium on field monitoring in geomechanics (ISFMG2022)*, London, UK.

Xu, X., Abadie, C. N., Möller, T., Della Ragione, G. & da Silva Burke, T. S. (2022b). On the use of high-resolution distributed fibre optic sensing for small-scale geotechnical experiments at 1*g*. *10th international conference on physical modelling in geotechnics (ICPMG)*, Daejeon, Korea.

Youssef, A. M., El-Kaliouby, H. & Zabramawi, Y. A. (2012). Sinkhole detection using electrical resistivity tomography in Saudi Arabia. *J. Geophys. Engng* **9**, No. 6, 655–663.

Zhang, C. C., Zhu, H. H. & Shi, B. (2016). Role of the interface between distributed fibre optic strain sensor and soil in ground deformation measurement. *Sci. Rep.* **6**, No. 1, 36469.